Journal of Biomedical Optics

BiomedicalOptics.SPIEDigitalLibrary.org

# Slope-based segmentation of articular cartilage using polarization-sensitive optical coherence tomography phase retardation image

Xin Zhou
Myeong Jin Ju
Lin Huang
Shuo Tang

SPIE.

Xin Zhou, Myeong Jin Ju, Lin Huang, Shuo Tang, "Slope-based segmentation of articular cartilage using polarization-sensitive optical coherence tomography phase retardation image," *J. Biomed. Opt.* **24**(3), 036006 (2019), doi: 10.1117/1.JBO.24.3.036006.

# Slope-based segmentation of articular cartilage using polarization-sensitive optical coherence tomography phase retardation image

**Xin Zhou,[a] Myeong Jin Ju,[b,c] Lin Huang,[a] and Shuo Tang[a,*]**
[a]University of British Columbia, Department of Electrical and Computer Engineering, Vancouver, British Columbia, Canada
[b]Simon Fraser University, School of Engineering Science, Burnaby, British Columbia, Canada
[c]Beckman Laser Institute-Korea, Dankook University, Cheonan, Chungnam, South Korea

**Abstract.** A segmentation method based on phase retardation measurements from polarization-sensitive optical coherence tomography (PS-OCT) is developed to differentiate the structural zones of articular cartilage. The organization of collagen matrix in articular cartilage varies over the different structural zones, generating different tissue birefringence. Analyzing the slope of the accumulated phase retardation at different depths can detect the variation in tissue birefringence and be used to segment the structural zones. The method is validated on phantoms composed of layers of different materials. Articular cartilage samples from adult swine are segmented with the method. The characteristics in each segmented zone are also examined by histology and high-resolution second-harmonic generation imaging, showing distinctive properties that match with the anatomical structure of articular cartilage. The segmentation algorithm is also applied on PS-OCT images acquired at multiple illumination angles, where the angular dependence of tissue birefringence in the deep zone is detected. This method offers a noninvasive imaging approach to differentiating the structural zones of articular cartilage, as well as a quantification approach based on the phase retardation measurements of PS-OCT. This method has great potential in studying depth-related progression of cartilage degeneration.  [DOI: 10.1117/1.JBO.24.3.036006]

Keywords: polarization-sensitive optical coherence tomography; phase retardation; segmentation; articular cartilage.

Paper 180555R received Sep. 18, 2018; accepted for publication Jan. 2, 2019; published online Mar. 14, 2019.

## 1 Introduction

Articular cartilage is the tissue that covers the ends of bones in joints and facilitates the transmission of loads. It is composed of a dense extracellular matrix (ECM) of collagen. From the joint surface to the bone, articular cartilage can be divided into four structural zones: superficial zone, transitional zone, deep zone, and calcified zone.[1] Superficial zone makes up 10% to 20% of the cartilage thickness. It is the only zone that contains type I collagen which forms large fiber bundles aligned in parallel to the articular surface. Transitional (or middle) zone covers 40% to 60% of the cartilage thickness. It contains mostly type II collagen which forms collagen fibrils oriented obliquely to the surface. Deep zone and calcified zone together cover 20% to 50% of the cartilage thickness. Deep zone is composed mostly of type II collagen which forms small fibrils aligned perpendicularly to the articular surface. Calcified zone serves as an interface between hard bone and soft cartilage. It is also composed mostly of type II collagen, but with higher degree of mineralization.[2]

Osteoarthritis (OA) is the most common form of joint disease and is associated with the degeneration of cartilage ECM. The destruction and structural damage of ECM progress gradually from superficial zone toward deep zone as the severity of degeneration increases.[3] To diagnose the severity of cartilage degeneration, it is important to differentiate the different cartilage structural zones. An imaging and segmentation method that can detect the different structural zones can have many applications in diagnosing and repairing OA. Radiography and arthroscopy are the current standard imaging methods for diagnosing OA. Radiography measures joint space width, which can indicate the loss of cartilage. However, it lacks sufficient resolution for detecting early alterations in cartilage. Arthroscopy can only image cartilage surface but is unable to assess subsurface structures. Those current methods lack diagnostic accuracy, especially for early stage articular cartilage degeneration.

Optical coherence tomography (OCT) is a noninvasive real-time imaging technique, which can acquire the cross-sectional view of tissues. It has micrometer-scale spatial resolution and several millimeters of penetration depth. OCT detects tissue morphology through backscattered light. Using conventional OCT imaging, degenerative cartilage was found to show higher surface irregularity, less tissue homogeneity, and less penetration depth than healthy cartilage.[4,5] However, those morphological changes only occur when the degeneration is already severe. Using conventional OCT, Rogowska et al.[6] segmented the boundary between cartilage and bone. As conventional OCT only measures the intensity image of optical reflectivity in tissue, it cannot differentiate collagen variations in the different structural zones and thus lacks the sensitivity for detecting early cartilage degeneration.

Polarization-sensitive optical coherence tomography (PS-OCT) is a functional extension of conventional OCT. PS-OCT can characterize tissue birefringence by phase retardation measurement.[7–10] Tissue birefringence occurs in fibrous structures such as collagen fibers, where the optical refractive index along or perpendicular to the fiber direction is different. Such birefringence causes phase retardation between light polarized in those two orientations as light propagates through tissue.

*Address all correspondence to Shuo Tang, E-mail: tang@ece.ubc.ca

Tissue birefringence is very sensitive to collagen fiber organization, such as diameter, orientation, alignment, etc. As the organization of collagen ECM varies over different structural zones in articular cartilage, the tissue birefringence should also differ from zone to zone. Since PS-OCT has the capability to detect tissue birefringence, it has the potential to differentiate the structural zones.

In some early studies, reduced tissue birefringence was detected in degenerated cartilage due to severe alterations in collagen organization.[11,12] Those studies were still based on conventional OCT where the detection of reduced birefringence was qualitative and indirect. Later on, Ugryumova et al.[13] applied PS-OCT to image articular cartilage and measured tissue birefringence more directly by accumulated phase retardation. Xie et al.[3] utilized PS-OCT to image articular cartilage at different stages of degenerative joint disease (DJD), but found it was yet unable to distinguish the disease stage by qualitative observations from the PS-OCT phase retardation results. By PS-OCT, the tissue birefringence in articular cartilage was found to depend on not only the healthy states, but also the light illumination direction[14] and topographical location.[15] Therefore, a more comprehensive quantitative method is needed to distinguish the different severities of DJD. Brill et al.[16] quantified the features in the banding pattern of phase retardation image, such as the width and height of the bands and the total number of bands. Banding pattern appears when the phase retardation accumulates every $\pi$ phase shift. This approach is limited to tissues with strong birefringence as those with relatively weak birefringence cannot show the banding pattern, which makes it unsuitable for detecting early cartilage degenerations. Shyu et al.[17] utilized the slope of phase retardation image to quantify birefringence in articular cartilage. A single slope was quantified without the differentiation of structural zones. Multiple regions of interest (ROIs) over the cartilage tissue were analyzed, and the statistical results demonstrated different slope distributions for different disease states. However, there were still difficulties in detecting the specific characterizations and identifying the severity.

As the organization of collagen fibers varies over the different zones in articular cartilage, a better approach can be developed to detect such changes by characterizing the depth variation of tissue birefringence. A similar variation was observed in PS-OCT imaging of retina, where Duan et al.[18] detected almost constant phase retardation in choroid but rapid increase of phase retardation in sclera. They further segmented the chorio-scleral interface based on the change of the phase retardation slope. A theoretical study was carried out by Fanjul-Vélez and Arce-Diego[19] to simulate tissue birefringence in a layered structure using extended Jones matrix calculus. They built an ideal three-layer model for articular cartilage, where the collagen fibers were modeled as exactly parallel to the tissue surface in the superficial zone, in an arched shape in the transitional zone, and exactly perpendicular to the surface in the deep zone. Kasaragod et al.[20] adopted this model and compared experimental data with simulation. By fitting the experimental data with the simulation model, they obtained tissue parameters such as the thickness of the zones, birefringence, and the quadratic function representing the fiber orientation in the transitional zone. Their work showed that the three-layered cartilage structural zones could be extracted from PS-OCT phase retardation image. Nevertheless, their model system assumed ideal conditions of collagen fiber organization, which might not be realistic in practical conditions.

In this study, a segmentation method based on the slope of phase retardation is developed to differentiate the structural zones in articular cartilage from PS-OCT measurements. The method is validated on phantoms composed of multiple layers of materials with different birefringence. The method is then applied on swine articular cartilage to segment the superficial, transitional, and deep zones. The thickness and mean birefringence of each zone are quantified. The effect of illumination angle on the segmentation is also investigated. The characteristics of each segmented zone are further examined by histology and second-harmonic generation (SHG) imaging, which show distinctive features that match with the anatomical structure of articular cartilage. It is shown that this method is capable of differentiating the structural zones in articular cartilage, which can potentially improve the detection of early degeneration in articular cartilage.

## 2 Sample Preparation and Imaging Methods

### 2.1 *Phantom Design*

The purpose of a phantom study is to validate the segmentation method on phantoms made by well-defined layers of materials with different birefringence. Two phantoms are developed. Phantom 1 is made by tightly taping three layers of removable tape (Scotch® Magic™, 3M, 811) around a piece of cover glass (Fisherbrand™, 12-542-C). Removable tape has moderate birefringence, whereas cover glass has no birefringence. The thickness of a single layer of the tape is measured to be $53 \pm 1$ $\mu$m by an electronic digital caliper (Marathon, CO 030200). Phantom 2 is made by covering two layers of removable tape on top of chicken breast muscle. The birefringence of chicken breast muscle is typically two to three times higher than that of tape.

### 2.2 *Cartilage Tissue Preparation*

Articular bones from the knee joint of adult swine are obtained from a local farm and imaged within 24 h. Cartilage tissue blocks are extracted from the articular bone and cut into cubic blocks with edge length of around 3 to 5 mm. The top of the cubic tissue is the intact natural surface. In this study, PS-OCT imaging on five samples (S1 to S5) extracted from four animals is reported. The sample locations are illustrated in Fig. 1(a). All the samples are extracted from the distal femoral condyle. Samples S1, S2, S4, and S5 are extracted from the medial central location (position 1) of four different animals. Sample S3 is extracted from the lateral central location (position 2) of the same animal as S2. Thus, samples S2 and S3 compare two symmetric locations on the femoral condyle.

### 2.3 *Polarization-Sensitive Optical Coherence Tomography Imaging*

PS-OCT imaging is conducted on a previously reported PS-OCT system.[10] The schematic of the system is shown in Fig. 2. The system is based on a swept-source laser (Axsun Technologies Inc., Massachusetts), with the center wavelength of 1.06 $\mu$m, full width at half maximum bandwidth of 110 nm, and scanning rate of 100 kHz. The light from the source is split by a 90:10 single-mode optical fiber coupler, where the 90% port of the coupler is connected to a passive polarization delay unit, and the 10% port to the reference arm. With the

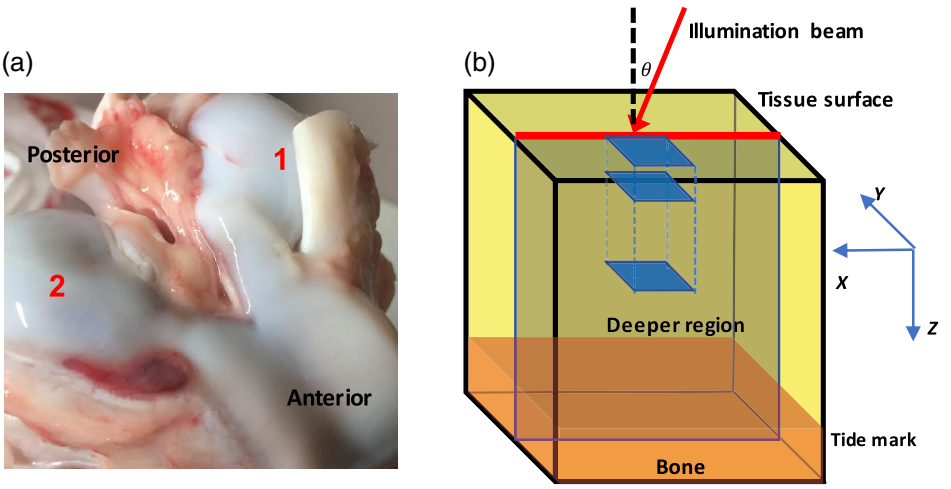


**Fig. 1** (a) Photograph of the articular bone sample. The numbers "1" and "2" mark the locations where the cartilage tissue blocks are extracted. (b) Laser illumination and image scanning configuration. Laser illuminates from the top on the tissue surface, and $\theta$ is illumination angle. In PS-OCT imaging, each A-line is along the $Z$ direction, a B-scan image is in the $XZ$ plane (large blue rectangle), and multiple B-scans are acquired along $Y$ axis. In SHG imaging, each frame is in the $XY$ plane (small blue rectangles), and an image stack can be acquired at different depths.

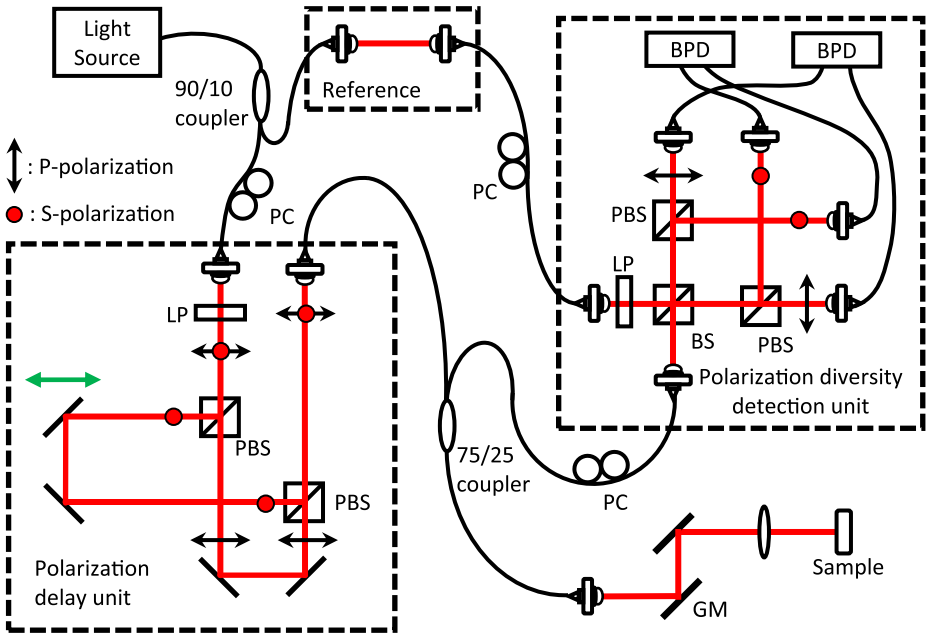


**Fig. 2** Schematic diagram of PS-OCT system. LP, linear polarizer; PC, polarization controller; GM, galvanometer scanner; BS, beam splitter; PBS, polarization beam splitter; BPD, balanced photodetector.

passive polarization delay unit, two orthogonal polarization states of light are separated and delayed in time. The light then passes through a 75:25 fiber coupler, and the 25% port is sent to illuminate the sample. The backscattered signal from the sample passes through the fiber coupler again, and the 75% port is sent to the detection unit. Light from the sample arm and the reference arm are guided to a polarization diversity (PD) detection unit. The polarization sensitive features are measured by a Jones-matrix-based method.[8,10] The average power on sample is around 2 mW. The depth resolution is ~8.1 $\mu$m in air, and the lateral resolution is ~19.2 $\mu$m.

The illumination and scanning geometry of PS-OCT imaging are shown in Fig. 1(b). The laser beam illuminates on the natural tissue surface from top. The incident angle $\theta$ is the angle between the laser beam and the normal of the tissue surface. Sample is attached on a tilting mount so that the incident angle $\theta$ can be adjusted in the azimuth plane ($XZ$ plane). At near normal incidence, $\theta$ is close to zero, and the beam is almost perpendicular to the tissue surface ($XY$ plane). At tilted illumination, $\theta$ is rotated around $Y$ axis. PS-OCT scanning is performed by scanning the laser beam in $X$ (fast scan) and $Y$ (slow scan) directions, with which a 3-D volume can be

acquired. Each B-scan image shows a cross-sectional view in the *XZ* plane.

In the PS-OCT system, two orthogonal input polarization states are illuminated on the sample, and two PD detectors measure the corresponding OCT output signals. Thus, the OCT output signals at each depth location $z$ can be written as a $2 \times 2$ matrix:

$$E_{\text{out}}(z) = \begin{bmatrix} E_{\text{A}}^{(1)}(z) & E_{\text{A}}^{(2)}(z) \\ E_{\text{B}}^{(1)}(z) & E_{\text{B}}^{(2)}(z) \end{bmatrix}, \tag{1}$$

where the superscripts 1 and 2 indicate the response to the input polarization states 1 and 2, respectively, and the subscripts A and B indicate the PD detectors A and B, respectively.

A surface segmentation is then applied to obtain the depth position $z_0$ of the sample surface and the corresponding $E_{\text{out}}(z_0)$. A similar matrix $M$ of the round-trip Jones matrix of the sample can be constructed as

$$M = E_{\text{out}}(z)E_{\text{out}}(z_0)^{-1} = \chi J_{\text{out}} J_s(z) J_{\text{out}}^{-1} \chi^{-1}, \tag{2}$$

where $J_s$ is the round-trip Jones matrix of the sample, $J_{\text{out}}$ is the Jones matrix from the sample surface to the PD detection unit, and $\chi$ represents the imperfection of the PD detection. By calculating the similar matrix $M$, the effect from the matrix $J_{\text{out}}$ and $\chi$, which can be regarded as the system-induced polarization impact, can be eliminated. The eigenvalues of $J_s$ should be the same eigenvalues $\lambda_{1,2}$ of $M$ due to the property of similar matrix.

The round-trip phase retardation of the sample, $\delta(z)$, is then obtained as the phase difference between the two eigenvalues as

$$\delta(z) = \begin{cases} \text{Arg}[\lambda_1 \lambda_2^*]: & 0 \le \text{Arg}[\lambda_1 \lambda_2^*] \le \pi \\ \text{Arg}[\lambda_1^* \lambda_2]: & \text{otherwise} \end{cases}. \tag{3}$$

### 2.4 *Second-Harmonic Generation Imaging*

Details about the SHG imaging system can be found in Ref. 21. A femtosecond Ti:sapphire laser is used to excite the nonlinear signal. A 60× objective lens with NA = 1.2 (UPLSAP060XW, Olympus) is used to acquire high-resolution imaging. The lateral resolution of the SHG imaging is 0.4 $\mu$m. Each SHG image frame is acquired in the *XY* plane as marked by the blue rectangles in Fig. 1(b). The field of view is ~130 $\mu$m × 130 $\mu$m. Two image stacks are acquired along the tissue depth (*Z* axis) by depth scanning. One stack is taken from the natural tissue surface into ~200-$\mu$m depth, and the other stack is taken after a ~0.5 mm of the top layer of the tissue is removed.

## 3 Phantom Study

The slope-based segmentation is first tested on phantoms composed of layers of different materials. Figure 3 shows the PS-OCT results for phantom 1, which contains three layers of tape, a piece of cover glass, and three layers of tape again. By PS-OCT imaging, coregistered intensity image and phase retardation image are obtained simultaneously. The intensity B-scan image is shown in Fig. 3(a). For each individual layer of tape, relatively strong back reflection can be obtained

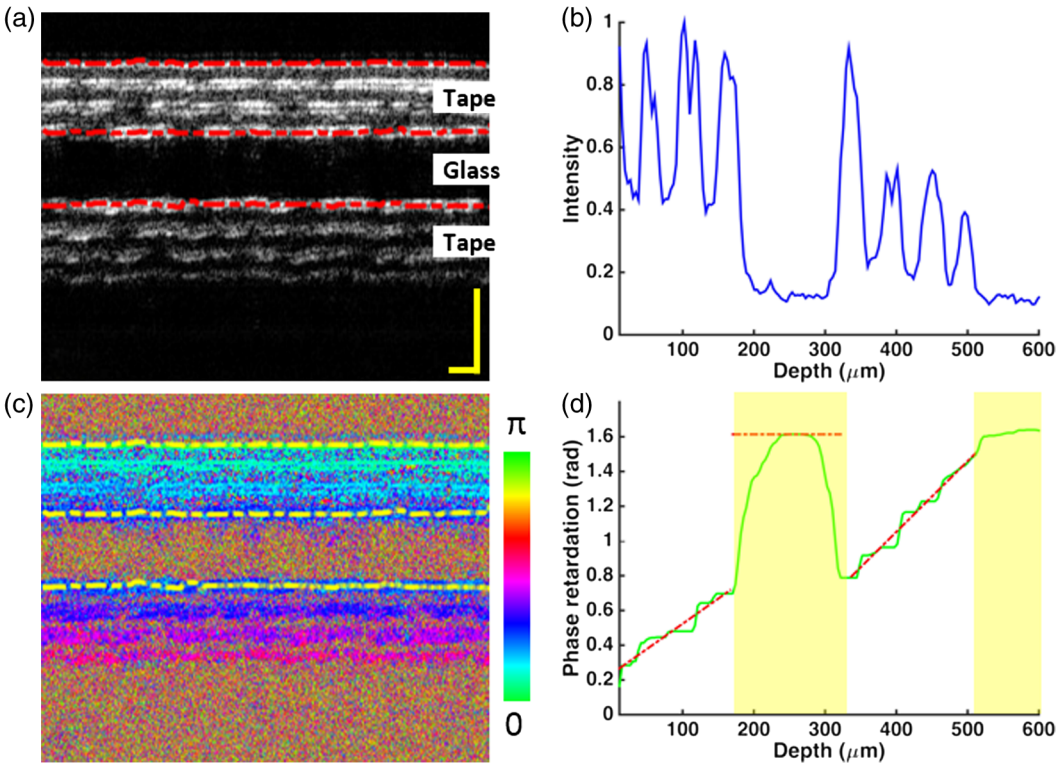


**Fig. 3** PS-OCT results for phantom 1. (a) Intensity image, (b) averaged intensity A-line profile, (c) phase retardation image, and (d) averaged A-line profile of accumulative phase retardation. Segmentation boundaries are marked by dashed lines in (a) and (c). Red dashed lines in (d) indicate the fitting results. Regions with low effective SNR (ESNR) is marked by yellow shadow. Scale bar is 200 $\mu$m.

from both its upper and lower boundaries. Three zones that are tape–glass–tape can be clearly distinguished in Fig. 3(a). In the top and bottom tape zones, three layers of tape can be seen. Figure 3(b) shows an averaged A-line profile. The peaks correspond to strong back reflection from each layer of the tape in the top and bottom tape zones, respectively. Therefore, from the intensity image, the boundaries between the zones can be clearly visualized.

The corresponding coregistered phase retardation B-scan image is shown in Fig. 3(c), and an averaged A-line profile of the accumulated phase retardation is shown in Fig. 3(d). In Fig. 3(d), it can be observed that the phase retardation increases linearly at the beginning, plateaus in the middle, and increases linearly again. The two linear regions correspond to the top and bottom tape zones, respectively, which show moderate birefringence. Phase retardation accumulates consistently and linearly in those two tape zones. On the other hand, cover glass has no birefringence, and the plateau profile in the middle region shows no accumulation of phase retardation. A ~1.6-rad phase retardation bias is observed in the plateau area. This kind of bias has also been reported by other groups[22] and is likely caused by averaging random-phase noise in a low signal-to-noise ratio (SNR) region, such as in the glass.

Slope-based segmentation is applied on the phase retardation A-line to find the boundaries between the zones. The two linear regions are segmented by searching the sudden change points (peaks in the second derivative curve) along a phase retardation A-line. The segmentation is obtained from each A-line for a ROI of 3 mm × 3 mm. The segmented boundaries are marked by the dashed lines in Fig. 3(c), corresponding to the phantom surface, boundary between the top tape zone and the cover glass, and boundary between the cover glass and the bottom tape zone, respectively. The same segmented boundaries are also marked in Fig. 3(a) and compared with the intensity image. As we can see, the segmented boundaries match very well with the visible interfaces in the intensity image. The averaged slope is found to be $0.178 \pm 0.023$ deg/$\mu$m in the top tape zone and $0.206 \pm 0.029$ deg/$\mu$m in the lower tape zone, respectively. The cover glass has no birefringence, where the phase retardation curve is fitted by a flat line. The thickness of the top tape zone (assuming $n = 1.3686$) is $162.1 \pm 6.4$ $\mu$m from the segmentation results, which is consistent with the measured value of ~159 $\mu$m by the caliper. The thickness of the cover glass (assuming $n = 1.5001$) is $154.1 \pm 9.9$ $\mu$m from the segmentation results, which matches well with the measured value of ~155 $\mu$m by the caliper.

Figure 4 shows the results from phantom 2, which contains two layers of tape on top of chicken breast tissue. The B-scan image and averaged A-line profile of the intensity signal are shown in Figs. 4(a) and 4(b), respectively, where the surface of the phantom and the boundary between the tape and chicken breast tissue can be clearly visualized. The B-scan image and averaged A-line profile of the phase retardation signal are shown in Figs. 4(c) and 4(d), respectively. In Fig. 4(d), two linear regions can be observed, a slower slope at the beginning and a faster slope at deeper depth. A two-segment linear fitting is applied to fit the phase retardation depth profile. The segmentation boundaries are obtained for a ROI of ~3 mm × 3 mm. The segmentation boundaries are marked as dashed lines in Figs. 4(a) and 4(c). As we can see, the segmentation boundaries match very well with the visible interfaces in the intensity image, corresponding to the surface of the phantom and the

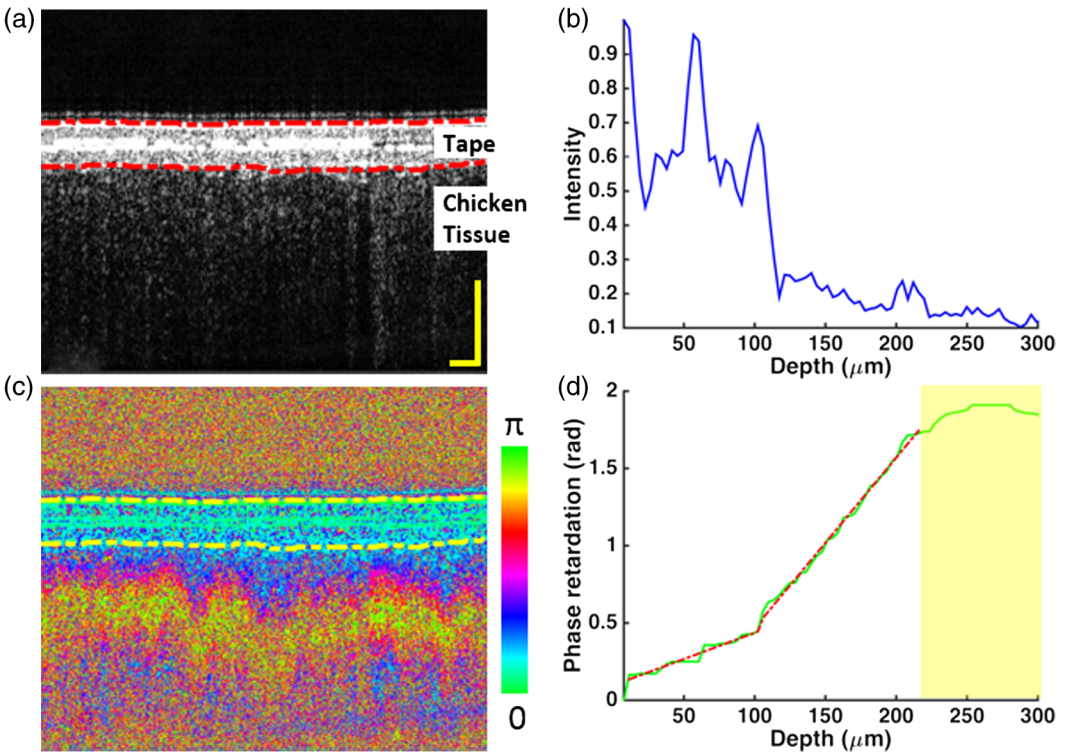


**Fig. 4** PS-OCT results for phantom 2. (a) Intensity image, (b) averaged intensity A-line profile, (c) phase retardation image, (d) averaged A-line profile of accumulative phase retardation. Segmentation boundaries are marked by dashed lines in (a) and (c). Red dashed lines in (d) indicate the fitting results. Region with low ESNR is marked by yellow shadow. Scale bar is 200 $\mu$m.

boundary between the tape and chicken tissue. The slope is found to be $0.183 \pm 0.029$ deg/$\mu$m in the tape zone and $0.573 \pm 0.097$ deg/$\mu$m in the chicken breast tissue, respectively. The birefringence in the chicken breast tissue is about three times higher than that in the tape. Through the phantom study, it is validated that phase retardation slope can be utilized to segment structural zones with different birefringence.

## 4 Cartilage Imaging

The slope-based segmentation method is next applied to cartilage tissues. The various zones in articular cartilage have different collagen organizations, which can result in different birefringence. Thus, multiple layers could be differentiated and segmented based on this property.

### 4.1 *Data Processing of Slope-Based Segmentation*

The segmentation algorithm is demonstrated on cartilage sample S1 as shown in Fig. 5. Figures 5(a) and 5(b) show the intensity and phase retardation image, respectively. The phase retardation is calculated based on the method described in Sec. 2.3. Details about the data processing are explained below.

**Preprocessing:** In Fig. 5(a), the tissue surface is clearly shown in the intensity image due to strong backscattering. The tissue surface is identified based on the intensity image and marked as *S* in the coregistered phase retardation image, as shown in Fig. 5(b). The origin of each A-line is defined at the surface of the tissue. Each A-line in the phase retardation image is then shifted up to flatten the surface. Running averaging is performed on each A-line by averaging it with its surrounding A-lines. The averaging window is selected as 21 A-lines by 11 B-scans by trial and error. Figure 5(c) shows a representative averaged phase retardation A-line, which shows a characteristic feature of multiple linear regions along the depth. From Fig. 5(c), three regions can be observed. The first region has a relatively flat slope and is located at the depth <200 $\mu$m; the second region has a slow slope and is located around the depth 200 to 400 $\mu$m; and the third region has a fast slope and is located at the depth >450 $\mu$m. A multi-segment linear fitting will be used to fit the phase retardation A-line.

**Reliability thresholding:** In the intensity images, SNR drops significantly at deep depth due to light attenuation, which can affect the reliability of the analysis. Effective signal-to-noise ratio (ESNR) is specific for Jones-matrix-based PS-OCT imaging,[22] which balances the SNR in the four channels acquired using two input polarization states and two PD detectors ($2 \times 2 = 4$). To ensure reliable calculation, thresholding is applied and pixels with ESNR <10 dB in the phase retardation image are removed.

**Slope-based segmentation:** Segmentation of the multiple linear regions is demonstrated on the phase retardation A-line shown in Fig. 5(c) as an example. In the segmentation process, the pixel positions *S*, B0, B1, B2, and *T* are solved for each phase retardation A-line, where *S* is the tissue surface, B0 and *T* are the starting and ending point, respectively, of the reliable phase retardation accumulation, B1 is the boundary between the superficial and transitional zone, and B2 is

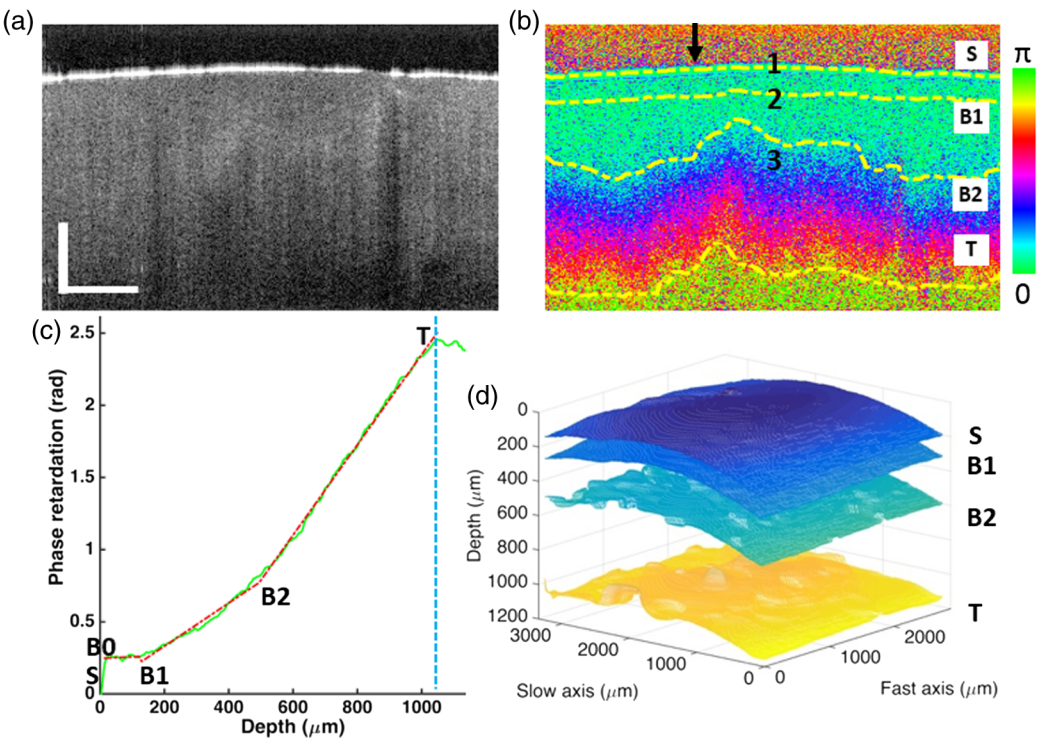


**Fig. 5** Segmentation results of articular cartilage sample S1 from the slope-based analysis in PS-OCT. (a) Intensity image and (b) phase retardation image. The 2-D segmented boundaries are marked by dashed lines and labeled as *S*, B1, B2, and *T*. (c) Averaged A-line profile of phase retardation, with fitting result shown in red dashed line. Blue dashed line indicates the reliable thresholding depth. (d) 3-D rendering of the segmentation results. Arrow in (b) indicates the location of the A-line shown in (c). Scale bar is 500 $\mu$m.

the boundary between the transitional and deep zone. Several assumptions are applied in the algorithm based on prior knowledge about articular cartilage: articular cartilage contains three structural zones, the superficial zone has a thickness <200 $\mu$m, and the PS-OCT imaging depth can reach the deep zone. Here, B0 is introduced to exclude the first, a few pixels which are highly fluctuating due to surface effect and artifacts. The following steps are taken in the segmentation algorithm:

1. Tissue surface $S$ is extracted by an automatic surface segmentation algorithm applied on the intensity B-scan image. The position of $S$ is then defined as the origin (pixel number 0) in the averaged A-line.
2. The maximum depth position, $T$, is determined by the reliability thresholding process. Considering the penetration depth and cartilage anatomy, $T$ typically reaches the deep zone.
3. Points B0 and B1′ (an initial position of B1) are solved together by a traversing search, where $\mathrm{B0}(i)$ is searched between pixel numbers 1 to 5 and $\mathrm{B1}'(j)$ is searched between pixel numbers $\mathrm{B0}(i)+5$ to 50. Each pixel length is calibrated to be ~3.7 $\mu$m. This range is determined by the prior knowledge that the thickness of the superficial zone is between 20 and 200 $\mu$m. For each pair of $\{i,j\}$, linear regression is applied to fit the phase retardation curve in the segment $\mathrm{B0}(i)-\mathrm{B1}'(j)$. The points B0 and B1′ are determined by minimizing the root-mean-square deviation of the liner regression.
4. Points B1 and B2 are also solved together by a traversing search, where $\mathrm{B1}(i)$ is searched within pixel number $\mathrm{B1}'\pm 5$ and $\mathrm{B2}(j)$ is searched between pixel number $\mathrm{B1}(i)+1$ to T-20. For each pair of $\{i,j\}$, linear least squares regression is conducted on the segments $\mathrm{B0}-\mathrm{B1}(i)$, $\mathrm{B1}(i)-\mathrm{B2}(j)$, and $\mathrm{B2}(j)-T$, simultaneously. The solution of B1 and B2 is determined by minimizing the total absolute error, equivalent to the least absolute deviation, over the three fitted regions.

From the segmentation, three regions with different phase retardation slopes can be distinguished as R-1 ($S-\mathrm{B1}$), R-2 (B1–B2), and R-3 ($\mathrm{B2}-T$), corresponding to superficial, transitional, and deep zone, respectively.

**Quantification of birefringence:** The depth position and thickness of each region can be extracted and quantified from the segmentation. Birefringence is quantified by the slope of the phase retardation curve. For tissue of thickness $z$, the round-trip phase retardation accumulation can be expressed as $\delta(z)=4\pi\Delta n\cdot z/\lambda_0$, where $\lambda_0$ is the central wavelength. From the linear fitting, the slope of the phase retardation accumulation can be extracted. The slope of the phase retardation is related to the birefringence $\Delta n$, as slope $=\frac{\mathrm{d}\delta(z)}{\mathrm{d}z}=\frac{4\pi\Delta n}{\lambda_0}$.[9,14] In this study, the optic axis of the collagen fiber is unknown. Thus, the obtained birefringence should be apparent birefringence, which will be discussed in more details later. By analyzing the accumulated phase retardation and quantifying its slope over a sufficient depth range, the accumulative properties of birefringence will be obtained and used to distinguish different structural zones.

### 4.2 *Slope-Based Segmentation in Articular Cartilage*

Figure 5 shows the PS-OCT imaging and segmentation results on sample S1 near normal illumination. The intensity and phase retardation images are shown in Figs. 5(a) and 5(b), respectively. Although the intensity image can show the tissue surface, it cannot differentiate the different structural zones. The phase retardation image shows the accumulated phase retardation along the depth. The color mapping corresponds to phase change over $0-\pi$. The band-like features indicate how the accumulated phase retardation changes, which cannot be observed in the intensity image. A representative phase retardation A-line from the B-scan image is shown in Fig. 5(c). The multisegment linear fitting results are shown as the red dashed segments. The boundaries $S$ (surface) and $T$ (maximum reliable depth) and the turning points B1 and B2 are marked. Three regions are segmented based on the multisegment linear fitting of the phase retardation A-line. From $S$ to B1, the phase retardation has not much accumulation in this short region near the surface (typically around 100 $\mu$m). From B1 to B2, the phase retardation starts to accumulate gradually. From $\mathrm{B2}-T$, the phase retardation increases at a relatively fast speed. The segmentation algorithm is applied to a 3-D image volume (300 A-lines in the fast axis and 200 B-scans in the slow axis, around 3 mm × 4 mm) to segment the zones. The segmentation results are rendered in 2-D and 3-D, respectively, in Figs. 5(b) and 5(d). The layers in the 3-D rendering show the zone divisions. The global features match with the geometrical shape of the tissue, with some topographically dependent variations.

Similar segmentation results have been obtained from other samples. Figure 6 shows the results from sample S2 (left column) and S3 (right column). From top to bottom, the intensity image, phase retardation image, and phase retardation A-line are shown, respectively. The segmented boundaries are marked by the dashed lines in the phase retardation images. Comparing Figs. 5 and 6, we can see that samples S2 and S3 show similar features as S1, where the superficial zone has a relatively flat slope and the deep zone has a faster slope than the transitional zone.

The averaged thickness and slope of each segmented region from the 3-D volume of the samples S1 to S3 are summarized in Table 1. Thickness is converted from optical path length by assuming an average refractive index $n=1.444$ in articular cartilage.[23] For sample S1, region R-1 is relatively thin with a thickness of ~125 $\mu$m. Region R-2 is twice thicker than R-1, which is consistent with the anatomical knowledge about the thickness of superficial and transitional zones.[1,2] Region R-3 is ~560-$\mu$m thick, and it may not represent the full thickness of the deep zone as the maximum reliable depth is limited by the light penetration. In relatively deep depth (>1 mm), the phase retardation computation becomes less reliable due to low SNR.[24] All the three samples have similar thickness division over the three regions. Especially, samples S2 and S3 show very close thickness in both regions R-1 and R-2. This indicates that the symmetric locations on the same cartilage sample have similar structural zone thickness.

In Table 1, the slopes of samples S1, S2, and S3 show some common characteristics. The slope increases from region R-1 to R-3. The slope in region R-1 is close to zero, with a large standard deviation that is higher than its mean value. This indicates that the phase retardation cannot accumulate sufficiently in region R-1, due to the frequent change of collagen fiber

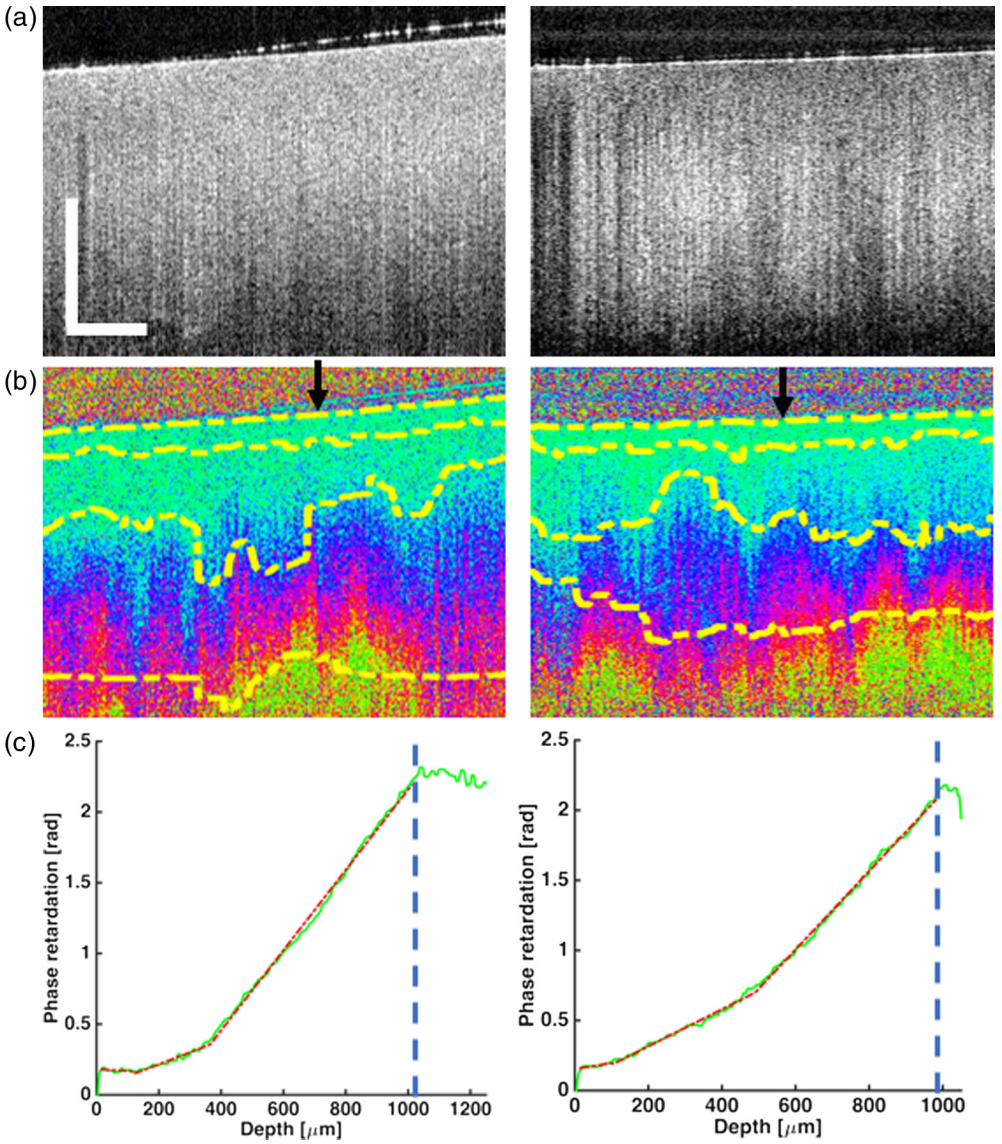


**Fig. 6** Segmentation results from articular cartilage sample S2 (left column) and S3 (right column). (a) Intensity image and (b) phase retardation image. Segmented boundaries are marked by dashed lines. (c) Averaged A-line profile of phase retardation, with the fitting result shown in red-dashed line. Blue-dashed line indicates the reliable thresholding depth. Arrow in (b) indicates the location of the A-line shown in (c). Scale bar is 500 $\mu$m.

**Table 1** Averaged thickness and phase retardation slope of segmented regions in samples S1, S2, and S3.

| | S1 | | S2 | | S3 | |
|---|---|---|---|---|---|---|
| Region | Thickness ($\mu$m) | Phase retardation slope (deg /$\mu$m) | Thickness ($\mu$m) | Phase retardation slope (deg /$\mu$m) | Thickness ($\mu$m) | Phase retardation slope (deg /$\mu$m) |
| R-1 | $125 \pm 9$ | $0.009 \pm 0.052$ | $107 \pm 20$ | $0.008 \pm 0.021$ | $106 \pm 29$ | $0.006 \pm 0.023$ |
| R-2 | $271 \pm 69$ | $0.046 \pm 0.021$ | $314 \pm 99$ | $0.043 \pm 0.019$ | $308 \pm 67$ | $0.038 \pm 0.018$ |
| R-3 | $563 \pm 213$ | $0.157 \pm 0.045$ | $499 \pm 175$ | $0.167 \pm 0.032$ | $421 \pm 91$ | $0.170 \pm 0.054$ |

orientations in the superficial zone at different depths. The slope in region R-2 is higher than that in R-1 as collagen fibers become obliquely aligned in the transitional zone. The slope in region R-3 is about 3 to 4 times higher than that in R-2. Other cases have also been observed where the slope in the deep zone is relatively low, which are likely caused by variations in the topographical locations and illumination angles. More discussions will be provided in Sec. 5.

In our investigation, region R-2 normally shows higher fitting error than the other regions. For the phase retardation slope, the relative standard deviation compared with its average value is also higher in region R-2 than in region R-3. Those information may imply that the collagen orientation in the transitional zone is more random than that in the deep zone. The standard deviation in the superficial zone is high, likely due to a combination of several reasons, such as uneven surface, strong surface reflection, and large fiber bundles with alternating orientations at different depths.

### 4.3 *Validation with Histology Image*

The PS-OCT segmentation is also compared with histology. In this experiment, sample S4 is imaged by PS-OCT. Afterward, the sample is sent to a histology lab to obtain the histology image. The PS-OCT phase retardation image is shown in Fig. 7(a). Three regions R-1, R-2, and R-3 can be differentiated and segmented based on the slope of the phase retardation measurement. The segmentation boundaries are marked by the dashed lines. The histology image of the same sample is shown in Fig. 7(b). Although the histology image does not have sufficient resolution to resolve collagen fibers, the shape and orientation of chondrocytes can be visualized, showing distinct features in different structural zones. Based on the averaged segmentation depth identified in the phase retardation image, the regions are marked by the brackets on the left side of Fig. 7(b). From the regions R-1, R-2, and R-3, different features of the chondrocytes can be observed. Zoomed-in images from a

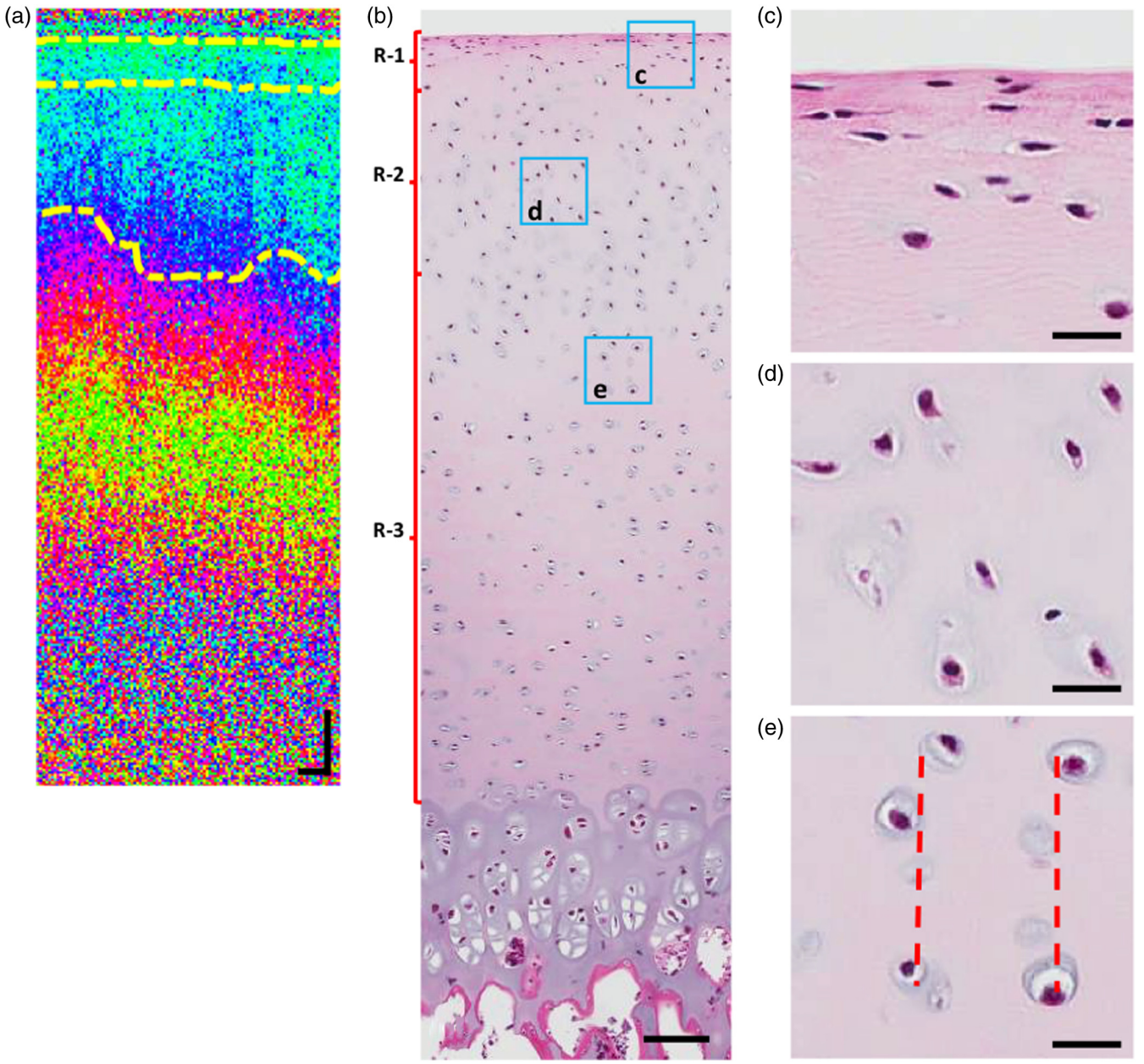


**Fig. 7** Comparison of PS-OCT with histology. (a) PS-OCT phase retardation image with segmented boundaries marked by dashed lines. (b) Histology image of the same sample. Scale bars in (a) and (b) are 100 $\mu$m; (c–e) Zoomed-in images from the ROIs indicated by the squares in (b). Red-dashed lines in (e) indicate the alignment of chondrocytes in columns. Scale bars in (c), (d), and (e) are 20 $\mu$m.

representative area selected from each region are shown in Figs. 7(c)–7(e), respectively. In Fig. 7(c), the chondrocytes are flattened and aligned almost parallel to the tissue surface. In Fig. 7(d), the chondrocytes are more rounded than in Fig. 7(c), and oriented obliquely. In Fig. 7(e), the chondrocytes are aligned in columns (the dashed lines indicate the approximate alignment of the chondrocytes). Those features in each selected region match with the common features of chondrocytes in the superficial, transitional, and deep zone of articular cartilage, respectively.[1,25] Thus, with the evidence from the histology results, the three segmented regions correspond to the superficial zone (R-1), transitional zone (R-2), and deep zone (R-3).

### 4.4 *PS-OCT Imaging Under Various Illumination Angles*

PS-OCT measurement has been reported to be sensitive to the illumination angle with respect to the collagen fiber orientation.[13,14,24,26] A multiple illumination angle study is performed on Sample S5 to further verify the multisegment slope-based segmentation in PS-OCT. Figure 8 shows the PS-OCT intensity and phase retardation images at illumination angles of −40 deg, −35 deg, −25 deg, −10 deg, 0 deg, 10 deg, 15 deg, 30 deg, and 40 deg. The banding structure in the color mapping can be used as a qualitative criterion, where tighter bands indicate higher tissue birefringence. The figures show that the tissue birefringence becomes higher as the illumination angle increases from 0 deg to larger angles.

To verify how the slope-based segmentation can also be applied to tilted illumination, three A-line profiles and the corresponding multisegment linear fitting are shown in Figs. 9(a)–9(c), at illumination angles of around 0 deg, −25 deg, and −40 deg, respectively. The locations of the corresponding A-lines are marked by the arrows in the phase retardation images shown in Figs. 8(a), 8(c), and 8(e), respectively. In Fig. 9, the multisegment linear fitting works very well, and three regions are successfully segmented for each case at different illumination angles. From the surface to deep location, the phase retardation slope shows a minimum slope in region R-1, a slow slope in region R-2, and a fast slope in region R-3. Furthermore, the slope in region R-3 is sensitive to the illumination angle and it increases monotonically as the illumination angle increases from 0 deg to −25 deg and −40 deg.

The segmentation algorithm is applied on 3-D volume data at different illumination angles. The averaged segmentation depth and slope for each region are shown in Figs. 10(a) and 10(b), respectively. The averaged segmentation depth for B1, B2, and $T$ are ∼100, 500, and 1100 $\mu$m, respectively. Thus, the thickness of R-1, R-2, and R-3 are ∼100, 400, and 600 $\mu$m, respectively. In tilted illumination, light travels through a slightly longer path length in a layered structure compared with normal illumination. For the maximum tilting angle of ±40 deg, this difference is calculated to be ∼10% by considering refraction. In

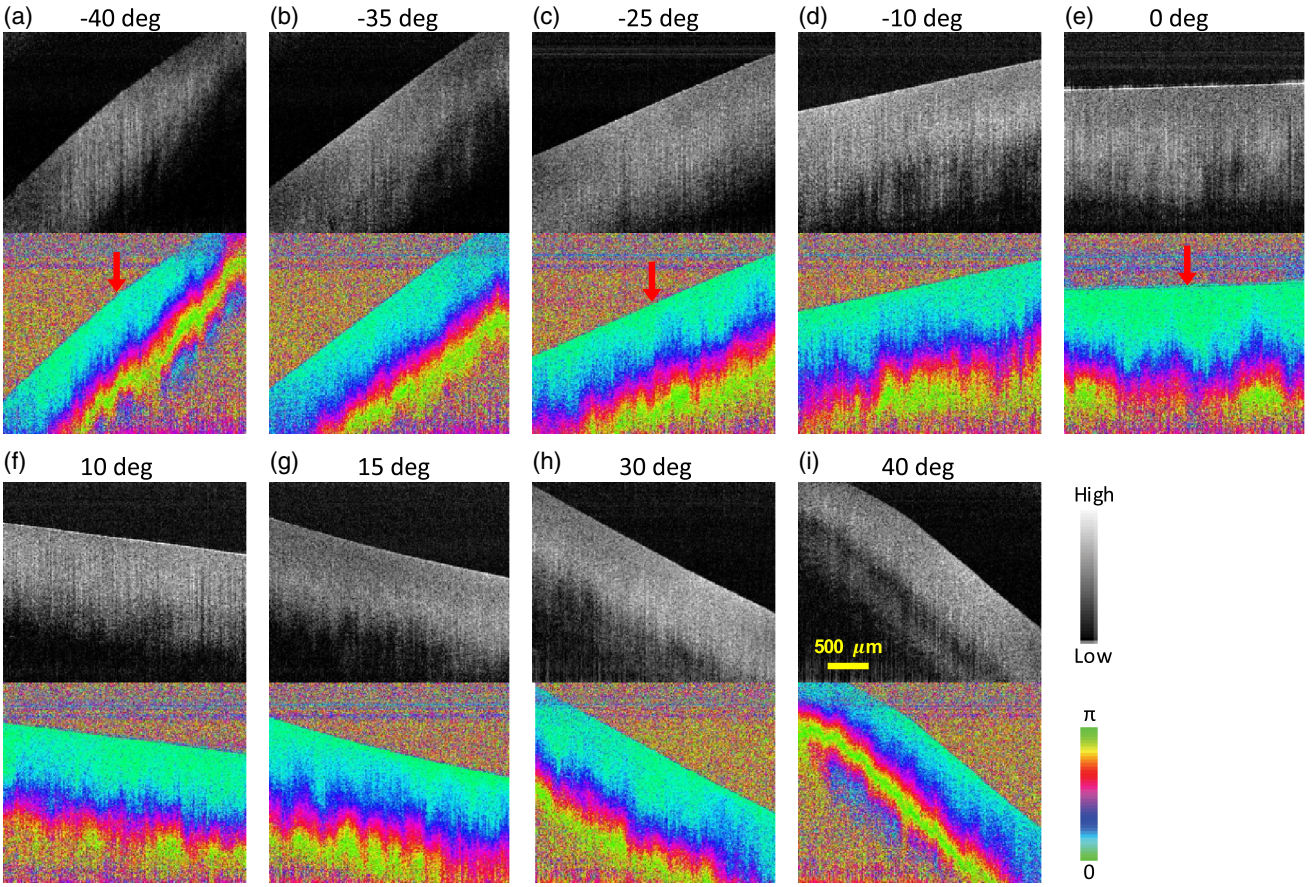


**Fig. 8** PS-OCT images measured at different illumination angles from −40 deg to 40 deg. In each B-scan image panel, the intensity OCT image is on the top, and the phase retardation image is at the bottom. The arrows indicate the locations of the A-lines. Scale bar is 500 $\mu$m.

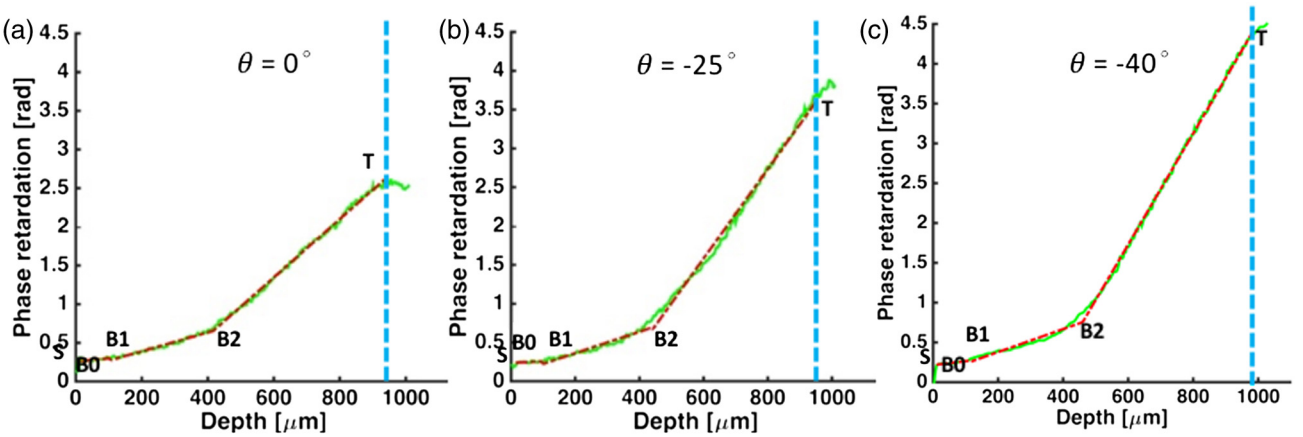


**Fig. 9** Phase retardation A-line profile at different illumination angles of $\theta = 0$ deg, $-25$ deg, and $-40$ deg, respectively. Fitting result is shown in red-dashed line. Blue-dashed line indicates the reliable thresholding depth.

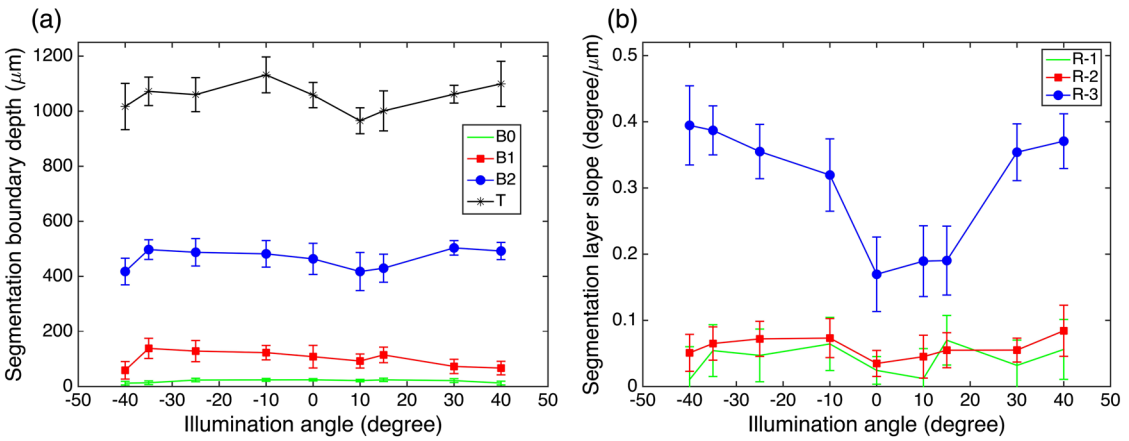


**Fig. 10** (a) Averaged boundary depths and (b) averaged phase retardation slopes of the segmented regions as a function of illumination angle.

Fig. 10(a), this small difference is not observed in the segmented layer thickness at different illumination angles likely because the variation of the structural zone thickness caused by topographical variation and tissue heterogeneity is >10%. Thus, in this study, the thickness is defined in the direction of the beam illumination for simplicity. At large tilting angles, the SNR is lower and the penetration depth is reduced, which can also be seen in the intensity images.

The averaged slopes of the different regions are shown in Fig. 10(b). Region R-3 has a larger slope than regions R-1 and R-2. It indicates that region R-3 has higher tissue birefringence. This is consistent with the anatomical fact that collagen fibers in the deep zone are densely packed and highly aligned.[2,25] The slope of region R-3 shows high sensitivity to the illumination angle. At 0 deg to 15 deg illumination angle, the slope is minimum at ~0.15 deg /$\mu$m. At $\pm 40$ deg, the slope is increased to ~0.4 deg /$\mu$m.

To understand the birefringence measured at different illumination angles, collagen fiber can be modeled as a uniaxial crystal. In a uniaxial crystal, the identical principal indices of refraction are called the ordinary index, $n_o$, and the distinctive index of refraction is called the extraordinary index, $n_e$. The index of refraction for the ordinary wave is simply $n_o$. The index of refraction for the extraordinary wave depends on the angle $\theta_c$ and is given as[27]

$$\frac{1}{n_e^2(\theta_c)} = \frac{\sin^2(\theta_c)}{n_e^2} + \frac{\cos^2(\theta_c)}{n_o^2}, \tag{4}$$

where $\theta_c$ is the angle between the direction of propagation and the optic axis. The true birefringence is defined as $|n_e - n_o|$. The apparent birefringence is defined as $\Delta n = n_e(\theta_c) - n_o$. In this study, the exact orientation of the optic axis is unknown and thus the measured birefringence should be apparent birefringence. When $\theta_c$ is 0 deg (propagating along the optic axis), the apparent birefringence becomes zero and no birefringence will be observed. When $\theta_c$ is 90 deg (propagating perpendicular to optic axis), the apparent birefringence reaches a maximum value which is the same as true birefringence.

In the deep zone, collagen fibers are aligned approximately in the perpendicular direction to the surface. When the illumination angle increases, a larger slope is observed, indicating higher apparent birefringence. As the collagen fibers may not be perfectly aligned and exactly parallel with the illumination light even at 0 deg tilting angle, some birefringence is still observed near normal illumination in our experiments. The

slopes in regions R-1 and R-2 are found to be not sensitive to the illumination angle. This is likely because the collagen fibers in the superficial zone change orientation at different depths, and the collagen fibers in the transitional zone are bent with some randomness.

### 4.5 *MPM Imaging of Articular Cartilage*

Although PS-OCT does not have sufficient resolution to directly visualize collagen fibers, SHG imaging is a high-resolution microscopy technique that can visualize the organization of collagen fibers. SHG imaging is carried out on sample S1 to examine the microscopic features at different depth regions. The microscopic features from the SHG imaging are then compared with the birefringence features measured by the PS-OCT for each structural zone.

Figure 11 shows the SHG images from approximately the three depths marked by 1, 2, and 3 in Fig. 5(b). Figures 11(a)–11(d) show SHG images at depth range 10 to 40 $\mu$m, near the tissue surface in region R-1. Large fiber bundles are clearly distinguished, and the fibers are almost parallel to the tissue surface. The fiber orientation changes from frame to frame at different depths. Those features match with the collagen properties in the superficial zone. With the fiber orientation changing frequently within a short depth range, the phase retardation cannot accumulate and the measured birefringence in this layer would be low. This is consistent with the relatively flat slope in region R-1 in the PS-OCT slope-based analysis. Figures 11(i)–11(l) show SHG images at depth around 500 to 600 $\mu$m, inside region R-3. The collagen in this region is found to form small fibrils that are densely packed. The dark circular holes correspond to chondrocytes that lack SHG contrast. Those features are consistent with the collagen properties in the deep zone, where type II collagen forms fibrils and the collagen density is high.[1] The orientation of the fibrils is hard to distinguish as limited by the resolution of the SHG imaging system. Figures 11(e)–11(h) show SHG images at depth range around 80 to 140 $\mu$m, in the transitional area from R-1 to R-2. The fibers are much smaller than those in the superficial zone, and they are not orientated in parallel with the surface, an indication of oblique orientation. The collagen density seems to be lower than that in the region R-3. Those features

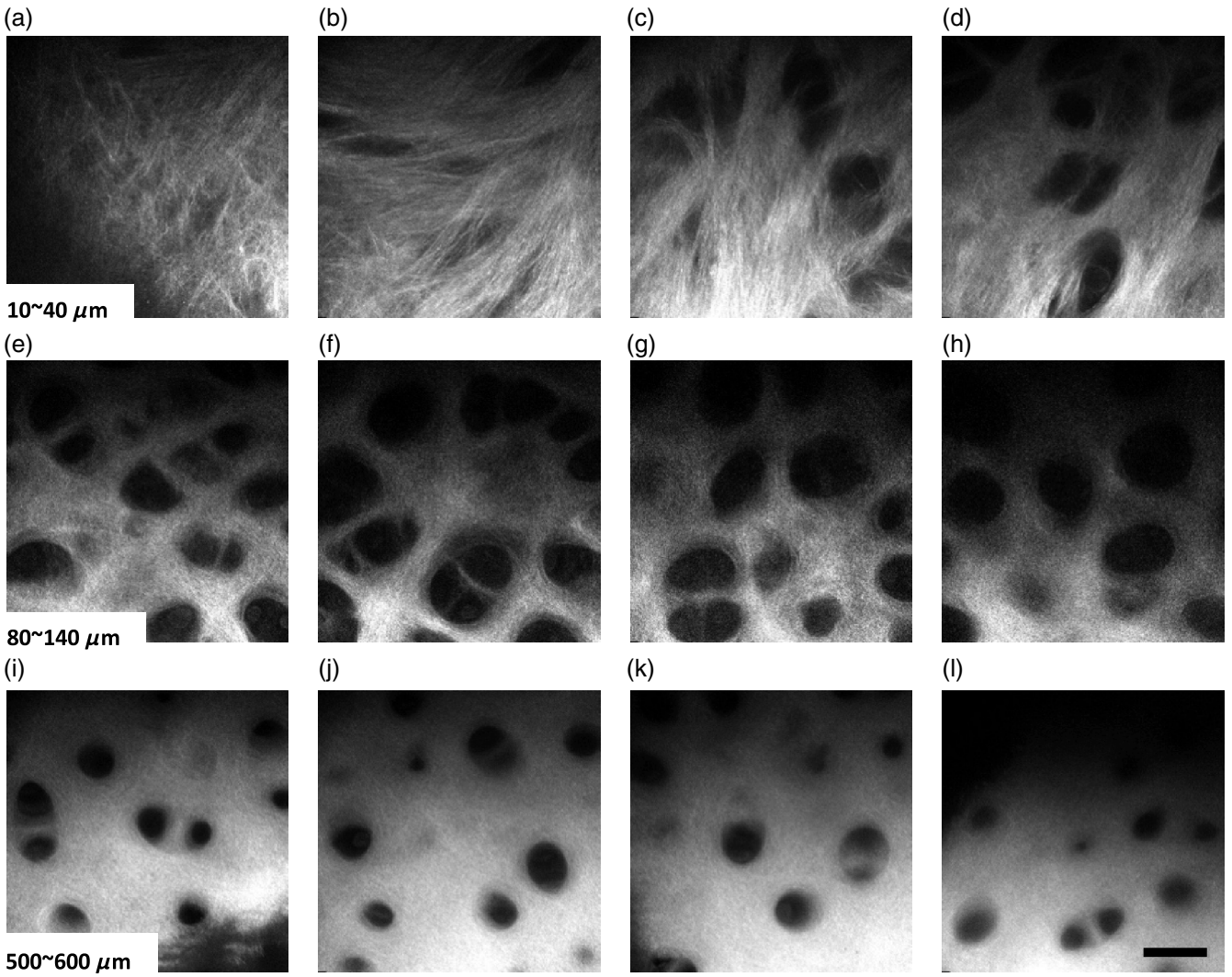


**Fig. 11** SHG images of articular cartilage. (a–d) SHG images at depths around 10, 20, 30, and 40 $\mu$m, in the superficial zone. (e–h) SHG images at depths around 80, 100, 120, and 140 $\mu$m, in the transitional zone. (i–l) SHG images at depths around 500 to 600 $\mu$m with 20-$\mu$m step size. Scale bar is 30 $\mu$m.

are consistent with the properties of the transitional zone. Thus, with the supportive evidence from high-resolution SHG imaging, the segmentations R-1, R-2, and R-3 from the PS-OCT analysis are shown to match with the characteristics of the superficial, transitional, and deep zone, respectively, in articular cartilage.

## 5 Discussion

In this study, relatively high birefringence is observed in the deep zone. Similar observations have also been reported by others that the phase retardation in the deep area may accumulate relatively fast in some locations of cartilage samples.[15,26] However, in some other reported literature,[14,16,20] low birefringence has been found in deep zone at normal incidence. The difference in the results shows that the quantification of birefringence in the deep zone is quite sensitive, and it may depend on the types of samples, topographical locations, illumination angles, etc. In our study, the knee joints of swine (4- to 6-months old) were used. In Ref. 14, the samples were extracted from the proximal tibia of adult Holstein dairy cows (5- to 7-years old). In Ref. 16, moderately degenerated cartilage samples were obtained from the central lateral femoral condyles of human patients.

In an ideal model where the collagen fibers are aligned perfectly perpendicular to the tissue surface in the deep zone, the birefringence should be low in the deep zone when the incident light is exactly parallel with the fiber orientation under normal incidence. However, in practice, real samples may differ from the ideal model. Studies with multiple measurement locations have shown that the major direction of collagen fibers is not exactly perpendicular to the surface and the angle may vary over locations.[13,15,28] From the measurements over a large area on joint surface, the orientation of collagen fibers in articular cartilage was observed to vary topographically,[28] where the collagen fibers in the deep area were not perpendicular to the tissue surface in the peripheral areas of the joint. Xie et al.[15] demonstrated similar topographical variations by measuring 30 locations on nine healthy bovine tibia samples by PS-OCT and polarized light microscopy (PLM). Among the 30 locations, 16 had shown relatively high birefringence in the deep area. Those samples were found to have tilted fiber orientation in the deep zone (not exactly perpendicular to the surface) observed by PLM. Ugryumova et al.[26] also found that the major collagen fiber orientation in the deep zone was not exactly perpendicular to the tissue surface.

In our experiment, the incident beam cannot be controlled to be aligned exactly parallel with the fiber orientation in the deep zone because the exact fiber orientation is unknown. Thus, it is likely that there is a nonzero angle between the illumination beam and the major collagen fiber orientation in the deep zone. Considering that the collagen fibers in the deep zone are highly aligned and densely packed, even a small angle could possibly result in a relatively high birefringence in the deep zone, which could still be higher than that in the transitional zone, depending on the fiber alignment and packing density in the two zones. From our measurements on multiple swine knee joints, the measured birefringence in the deep zone is usually higher than that in the transitional zone, which may represent a tilted collagen fiber orientation in the deep zone. Cases with relatively low measured birefringence in the deep zone are also observed but rare. It sometimes occurs in the central part of femoral cartilage but is usually limited within a localized area. For the locations demonstrated in this study, we have found similar segmentation results. They consistently show higher slope in deep zone than that in transitional zone. Noticeably, very tilted collagen fiber orientation was also reported from the articular cartilage of swine knee joint,[29] which is consistent with the cases in our study. Collagen fiber orientation in articular cartilage is complex and depends on the types of specimen and age,[29,30] joint and sampling location,[15,28] and other factors such as physical exercise and loading conditions. More studies are required to figure out the details in the future.

In this study, the measured phase retardation slope is related to the apparent birefringence, which is shown to be capable of differentiating the different structural zones in articular cartilage. Several references have reported on detecting the orientation of optic axis and true birefringence.[26,31] Reference 26 used a multiple angle illuminating strategy for measuring the optic axis in cartilage, where measurements with precisely symmetrical incident angles were required. Reference 31 measured the 3-D optic axis in cornea by utilizing extended Jones matrix formalism and prior knowledge of fiber orientation distribution in the sample. Both studies were based on free-space systems, with complex and precise control on the polarization state. Controlling polarization state in fiber-based system is more challenging. For future work, it will be interesting to investigate the detection of optic axis and true birefringence in articular cartilage using fiber-based PS-OCT system.

## 6 Conclusion

A segmentation method based on the slope of PS-OCT phase retardation measurement is developed to differentiate the structural zones of articular cartilage. The method is validated on phantoms composed of layers of different materials. Swine articular cartilage samples are segmented to differentiate the different structural zones. Typically, the superficial zone shows a relatively flat slope, the transitional zone shows a slow slope, and the deep zone shows a fast slope. The segmentation regions are further examined by histology and high-resolution SHG imaging, which show distinctive properties that match with the anatomical structures. The slope in the deep zone is found to be sensitive to the illumination angle, where the slope increases significantly with the illumination angle. As the slope of phase retardation is sensitive to and quantifies the tissue birefringence, this approach can detect changes in collagen ECM and thus segment the structural zones based on tissue birefringence. This method has great potential to characterize the progression of depth-dependent articular cartilage degeneration.

### *Disclosures*

The authors have no financial interests or potential conflict of interest to disclose concerning this work.

### *Acknowledgments*

The authors would like to thank Dr. Yoshiaki Yasuno for suggestions and advice. This project was supported by the Canadian Institutes of Health Research (CIHR)/Collaborative Health Research Projects (CPG-151974), the Natural Sciences and Engineering Research Council of Canada (NSERC)/Collaborative Health Research Projects (CHRP 508405-17), and the NSERC/Discovery Grants Program (RGPIN-2017-05913). Myeong Jin Ju also would like to appreciate the National Research Foundation of Korea (NRF-2018K1A4A3A02060572).

## References


1. A. J. S. Fox, A. Bedi, and S. A. Rodeo, "The basic science of articular cartilage: structure, composition, and function," *Sports Health* **1**(6), 461–468 (2009).
2. S. Camarero-Espinosa et al., "Articular cartilage: from formation to tissue engineering," *Biomater. Sci.* **4**(5), 734–767 (2016).
3. T. Xie et al., "Determination of characteristics of degenerative joint disease using optical coherence tomography and polarization sensitive optical coherence tomography," *Lasers Surg. Med.* **38**(9), 852–865 (2006).
4. S. Nebelung et al., "Morphometric grading of osteoarthritis by optical coherence tomography—an ex vivo study," *J. Orthop. Res.* **32**(10), 1381–1388 (2014).
5. S. Nebelung et al., "Quantitative OCT and MRI biomarkers for the differentiation of cartilage degeneration," *Skeletal Radiol.* **45**(4), 505–516 (2016).
6. J. Rogowska, C. M. Bryant, and M. E. Brezinski, "Cartilage thickness measurements from optical coherence tomography," *JOSA A* **20**(2), 357–367 (2003).
7. J. F. De Boer, C. K. Hitzenberger, and Y. Yasuno, "Polarization sensitive optical coherence tomography—a review," *Biomed. Opt. Express* **8**(3), 1838–1873 (2017).
8. B. H. Park et al., "Jones matrix analysis for a polarization-sensitive optical coherence tomography system using fiber-optic components," *Opt. Lett.* **29**, 2512–2514 (2004).
9. B. Cense et al., "In vivo birefringence and thickness measurements of the human retinal nerve fiber layer using polarization-sensitive optical coherence tomography," *J. Biomed. Opt.* **9**(1), 121–126 (2004).
10. M. J. Ju et al., "Advanced multi-contrast Jones matrix optical coherence tomography for Doppler and polarization sensitive imaging," *Opt. Express* **21**(16), 19412–19436 (2013).
11. X. Li et al., "High-resolution optical coherence tomographic imaging of osteoarthritic cartilage during open knee surgery," *Arthritis Res. Ther.* **7**(2), R318–R323 (2005).
12. C. R. Chu et al., "Clinical optical coherence tomography of early articular cartilage degeneration in patients with degenerative meniscal tears," *Arthritis Rheum.* **62**(5), 1412–1420 (2010).
13. N. Ugryumova et al., "The collagen structure of equine articular cartilage, characterized using polarization-sensitive optical coherence tomography," *J. Phys. D* **38**(15), 2612–2619 (2005).
14. T. Xie et al., "Use of polarization-sensitive optical coherence tomography to determine the directional polarization sensitivity of articular cartilage and meniscus," *J. Biomed. Opt.* **11**(6), 064001 (2006).
15. T. Xie et al., "Topographical variations in the polarization sensitivity of articular cartilage as determined by polarization-sensitive optical coherence tomography and polarized light microscopy," *J. Biomed. Opt.* **13**(5), 054034 (2008).
16. N. Brill et al., "Polarization-sensitive optical coherence tomography-based imaging, parameterization, and quantification of human cartilage degeneration," *J. Biomed. Opt.* **21**(7), 076013 (2016).
17. J. J. Shyu et al., "Diagnosis of articular cartilage damage by polarization sensitive optical coherence tomography and the extracted optical properties," *PIER* **91**, 365–376 (2009).
18. L. Duan, M. Yamanari, and Y. Yasuno, "Automated phase retardation oriented segmentation of chorio-scleral interface by polarization sensitive optical coherence tomography," *Opt. Express* **20**(3), 3353–3366 (2012).
19. F. Fanjul-Vélez and J. L. Arce-Diego, "Polarimetry of birefringent biological tissues with arbitrary fibril orientation and variable incidence angle," *Opt. Lett.* **35**(8), 1163–1165 (2010).
20. D. K. Kasaragod et al., "Experimental validation of an extended Jones matrix calculus model to study the 3D structural orientation of the collagen fibers in articular cartilage using polarization-sensitive optical coherence tomography," *Biomed. Opt. Express* **3**(3), 378–387 (2012).
21. S. Tang et al., "Imaging subcellular scattering contrast by using combined optical coherence and multiphoton microscopy," *Opt. Lett.* **32**(5), 503–505 (2007).
22. L. Duan et al., "Monte-Carlo-based phase retardation estimator for polarization sensitive optical coherence tomography," *Opt. Express* **19**(17), 16330–16345 (2011).
23. K. Wang, J. Wu, and T. B. Kirk, "Depth-dependent refractive index of normal and early degenerated articular cartilage," *J. Biomed. Opt.* **18**(10), 105003 (2013).
24. N. Ugryumova, S. V. Gangnus, and S. J. Matcher, "Three-dimensional optic axis determination using variable-incidence-angle polarization-optical coherence tomography," *Opt. Lett.* **31**(15), 2305–2307 (2006).
25. B. He et al., "High-resolution measurements of the multilayer ultrastructure of articular cartilage and their translational potential," *Arthritis Res. Ther.* **16**(2), 205 (2014).
26. N. Ugryumova et al., "Novel optical imaging technique to determine the 3-D orientation of collagen fibers in cartilage: variable-incidence angle polarization-sensitive optical coherence tomography," *Osteoarthr. Cartil.* **17**(1), 33–42 (2009).
27. J. M. Liu, *Photonic Devices*, Cambridge University Press, Cambridge, UK (2009).
28. Y. Xia et al., "Imaging the physical and morphological properties of a multi-zone young articular cartilage at microscopic resolution," *J. Mag. Reson. Imaging* **17**(3), 365–374 (2003).
29. M. J. Nissi et al., "T2 relaxation time mapping reveals age-and species-related diversity of collagen network architecture in articular cartilage," *Osteoarthr. Cartil.* **14**(12), 1265–1271 (2006).
30. M. M. Hyttinen et al., "Changes in collagen fibril network organization and proteoglycan distribution in equine articular cartilage during maturation and growth," *J. Anatomy* **215**(5), 584–591 (2009).
31. F. Fanjul-Vélez et al., "Polarimetric analysis of the human cornea measured by polarization-sensitive optical coherence tomography," *J. Biomed. Opt.* **15**(5), 056004 (2010).



**Xin Zhou** is a PhD student at the Department of Electrical and Computer Engineering from the University of British Columbia. He has been working in the field of bio-photonics for five years. His research interest is in the area of optical coherence tomography and related techniques. He is now studying on the development of polarization sensitive optical coherence tomography (PS-OCT) as well as seeking for its clinic applications.

**Myeong Jin Ju** is a postdoctor at the School of Engineering Science from Simon Fraser University. His research interest is in optical coherence tomography system development and related applications.

**Lin Huang** is currently a PhD candidate at the Department of Electrical and Computer Engineering from the University of British Columbia. Her research interest is in miniature multiphoton systems and devices and femtosecond fiber laser.

**Shuo Tang** is an associate professor at the Department of Electrical and Computer Engineering from the University of British Columbia. Her research interest is in biomedical optical imaging systems and devices, including multiphoton microscopy, optical coherence tomography, and microendoscopy systems for biomedical applications.